Article

High-precision time-domain stereoscopic imaging with a femtosecond electro-optic comb

Zijian Wang [1], Hui Ma[1], Jingwei Luo[1], Ming Yan [1,2] ✉, Kun Huang [1,2], Jianan Fang[1,2], Jinman Ge[3] & Heping Zeng [1,2,3,4] ✉

Stereoscopy harnesses two spatially offset cameras to mimic human vision for depth perception, enabling 3D optical imaging for various remote sensing applications. However, its depth precision and accuracy are limited by insufficient spatial resolving power. Achieving high precision alongside extensive measurable ranges and high-speed measuring capabilities has long been a challenge in 3D imaging. To address this, we introduce time-domain stereoscopy, a concept inspired by space-time duality in optics. Specifically, it employs two temporally offset optical gating cameras to capture time-domain parallax signals, enabling rapid and precise time-of-flight measurements for depth retrieval. Leveraging two advanced technologies—femtosecond electro-optical comb synthesis and nonlinear optical sampling—this method achieves sub-100-nanometer depth precision across multimeter-scale imaging ranges and supports millisecond-scale displacement and velocity measurements for 47 million spatial points simultaneously. As such, it provides a versatile tool for applications in surface metrology, mechanical dynamics, and precision manufacturing.

In optics, the parallels between concepts in the spatial and temporal domains, often referred to as space-time duality[1], have led to the development of many revolutionary photonic tools, impacting diverse fields of science and technology, including ultrafast physics, quantum optics, spectroscopy, microscopy, and signal processing. For example, the development time-stretch photonics[2,3], analogous to dispersing elements in space, has enabled powerful tools, such as wideband analog-to-digital converters and ultrafast signal processors, uncovering phenomena like optical rogue waves, relativistic electron bunching, and quantum chaos, and unlocking new opportunities for applications such as cancer detection, blood testing, optical computing, and 3D light detection and ranging (lidar)[4].

Inspired by this duality, we here devise a time-domain stereoscopic technique (TDS), enabling high-precision, large-dynamic-range, far-field 3D optical imaging. Initially, stereoscopic imaging is performed in the spatial domain, which mimics human eyes to perceive depth using two slightly offset cameras to capture two images of the same scene from different angles. The disparity between the two images yields a depth map, enabling 3D reconstruction[5]. While effective in fields like robotics and autonomous driving, stereo imaging is limited in axial resolution and accuracy due to insufficient spatially resolving capability, especially in low-contrast, reflective, or textureless environments.

Analogous to its spatial-domain counterpart, TDS uses two temporally offset cameras to capture two images from the same laser pulse reflected by a target (Fig. 1a). The disparity between these images manifests in the time domain (Fig. 1b), and this temporal difference, decisive for depth retrieval, is determined precisely and rapidly by leveraging advanced time-domain techniques such as ultrafast optical sampling. Consequently, TDS addresses two key challenges for 3D

[1]State Key Laboratory of Precision Spectroscopy, Hainan Institute, East China Normal University, Shanghai, China. [2]Chongqing Key Laboratory of Precision Optics, Chongqing Institute of East China Normal University, Chongqing, China. [3]National Key Laboratory of Science and Technology on Space Microwave, CAST Xi'an, Xi'an, China. [4]Jinan Institute of Quantum Technology, Jinan, Shandong, China. ✉e-mail: myan@lps.ecnu.edu.cn; hpzeng@phy.ecnu.edu.cn
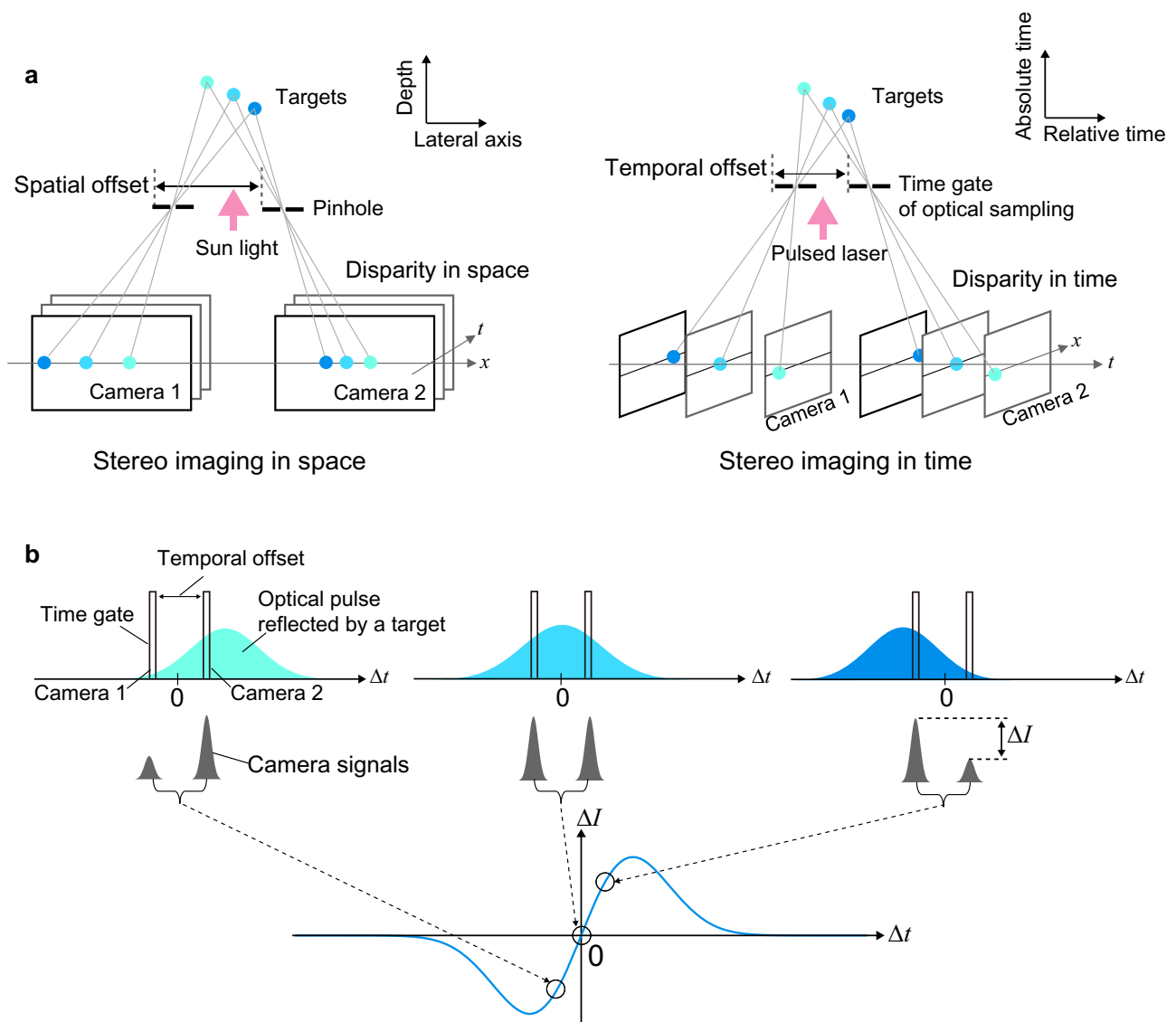
Fig. 1 | Concepts of TDS. a Simplified illustration of stereoscopy in space and in time. The light gray lines represent optical paths or time-of-flight. The symbols x and t correspond to space and time coordinates. **b** Optical sampling and time-domain disparities. In short, pulses arriving at different times produce different intensities on the two cameras. This intensity difference (ΔI), as a differential function of the pulses' arrival time (Δt) relative to the time zero (the center of the gates), is used to determine distance.

imaging[6–8]: (1) integrating high axial resolution and precision with an extended imaging range or depth-of-field (DOF); and (2) performing 3D measurements in a high-speed, real-time fashion. Overcoming these challenges is crucial for surface metrology, remote sensing, mechanical dynamics, and tasks like object recognition, navigation, and scene reconstruction, which have widespread applications in areas like advanced manufacturing, security, and defense[9,10].

As a brief introduction, existing 3D optical imaging techniques can be crudely divided into two groups. The first covers large measurement distances (from a few meters to hundreds of meters) but with limited depth resolution and precision (at the millimeter or centimeter levels), including techniques such as stereoscopic imaging, time-of-flight (ToF) ranging cameras[11], structured light projection[12], and the 3D lidar family[13–15]. The second achieves nanometer precision but is limited to short ranges or DOF (typically to just a few millimeters), including techniques like serial time-encoded amplified microscopic imaging[16], optical sampling imaging based on electro-optical or nonlinear effects[17–20], and interferometric imaging and tomography[21–24], primarily utilizing an interferometer with a moving arm. Meanwhile, the emergence of optical combs, a coherent light source precisely controlled in both time and frequency domains, opens up new opportunities for lidar[25–28] and high-dimensional imaging[29,30]. Particularly, dual-comb interferometry, without the limitation of moving parts, enables rapid, long-range absolute distance measurements via heterodyne detection of two mutually coherent combs[25]. This dual-comb concept has been successfully adopted for hyperspectral digital holography[29]. However, the requirement for two tightly locked coherent combs, along with the high computational load and low refresh rate, limits its applicability due to complexity, cost, and real-time constraints. Therefore, despite its importance, high-precision, large-range 3D imaging with real-time measurement capability has remained a missing element in the field. The TDS method we propose offers a promising solution to bridge this gap.

In this paper, we present the concept and setup of time-domain stereoscopic imaging, demonstrate its capabilities in remote 3D imaging, precision, and high-speed measurements, and conclude with performance comparisons and future prospects.
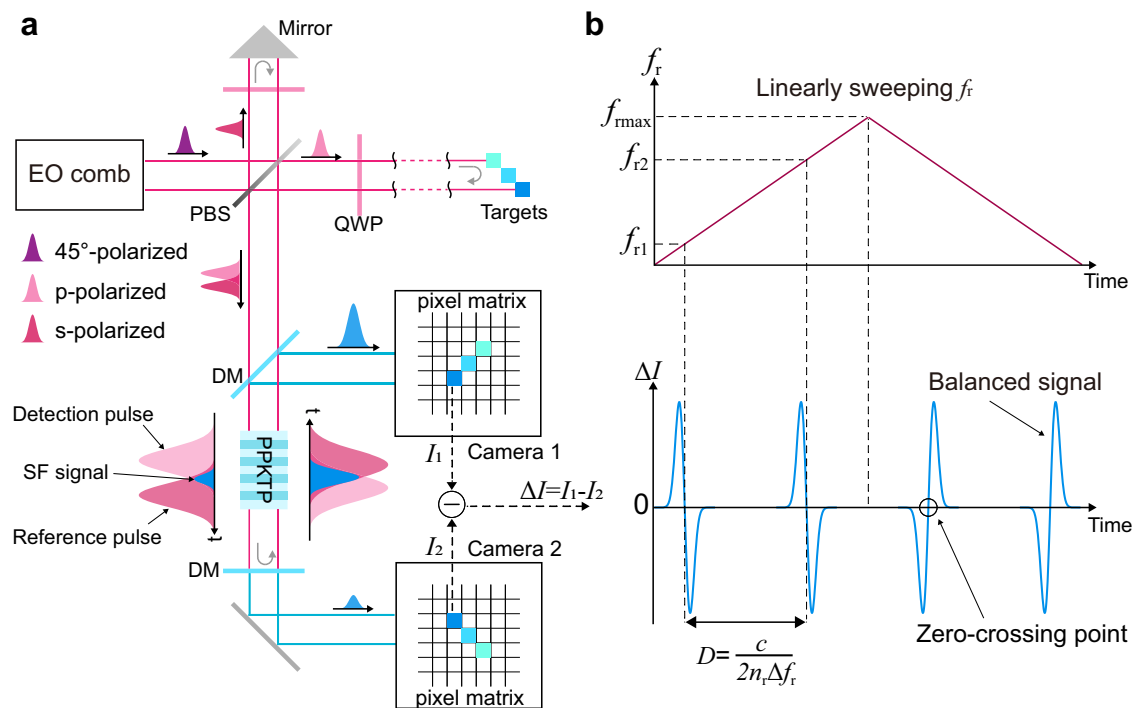
Fig. 2 | Schematics of TDS based on a balanced cross-correlator. a Balanced imaging with two optical sampling cameras. PBS, polarization beamsplitter; QWP, quarter wave plate; DM, dichroic mirror; PPKTP, periodically poled KTiOPO$_4$; I_1, I_2, electrical signal intensity for a pixel of camera 1 (camera 2). **b** Balanced signals as a function of repetition frequency (f_r) tuning of an electro-optical (EO) comb. In (**a**), an EO comb emits ultrashort optical pulses that travel to the target, reflect off surfaces, and return to a balanced cross-correlator. Inside this correlator, the orthogonally polarized detection and reference pulses pass through the PPKTP crystal twice, generating bidirectional sum-frequency signals as they temporally overlap inside the crystal. The sum-frequency beams then project two correlated images of a target onto the respective cameras, which are synchronized to the f_r tuning. By subtracting the intensities of two correlated pixels (each from a camera), one can derive the balanced signal (ΔI) at any spatial point. In (**b**), a target distance is calculated as $D = c/(2n_r \cdot \Delta f_r)$, where n_r, c, and Δf_r represent the reflective index of the air, the speed of light in a vacuum, and the frequency difference between two consecutive zero-crossing points (at f_{r1} and f_{r2}).

Results

Basic concept and principle

Figure 1a conceptually compares TDS with conventional stereo imaging (see details in Supplementary Fig. 1 and Supplementary Table 1). In both cases, achieving high depth precision and accuracy hinges on precisely measuring minute disparities. This task proves challenging in the space domain (fundamentally due to the diffraction limit); conversely, exploiting the time domain benefits from advancements in optical comb and precise timing technologies. Specifically, in TDS, a laser pulse reflected by a target is captured by two cameras gated with a slight temporal offset, yielding distinct electrical signals (Fig. 1b). This imbalance (ΔI) is governed by the temporal difference (Δt) between the pulse flight time (T_D) and the paired time gates, where $\Delta t = T_D - m/f_r$ and m/f_r represents a multiple of the repetition period of the gates (provided the two gates are synchronized). The pulse and the paired gates overlap optimally at a zero-crossing point (the middle case in Fig. 1b), where $\Delta t = 0$ and $T_D = m/f_r$. The integer $m = f_{r1}/\Delta f_r$, where $\Delta f_r = f_{r2} - f_{r1}$, is obtained in a stroboscopic fashion, as $m/f_{r1} = (m + 1)/f_{r2}$, given two adjacent zero-crossing points at f_{r1} and f_{r2}, with $f_{r1} < f_{r2}$. Consequently, a target distance (D) is determined as $D = c \cdot T_D/2n_r = c/(2n_r \cdot \Delta f_r)$, where n_r is the reflective index of the air and c is the speed of light in a vacuum. Note that there are two prerequisites: (1) timing the gates precisely, which is available using optical combs; (2) the gates shorter than or comparable to the laser pulse, achievable via optical gating.

A key advantage of TDS over a conventional ToF camera is its superior noise immunity. A similar analogy can be drawn when comparing single-detector cross-correlation with balanced cross-correlation (BCC) in laser synchronization experiments[31–33]. The balanced one significantly improves timing precision to the attosecond level, surpassing the former by orders of magnitude, through the

elimination of common-mode optical and electrical noise. This advantage also applies to TDS, rendering it inherently sensitive to minute changes in time as well as in distance—a core feature of this approach. Note that the BCC scheme has been adopted for high-precision single-point rangefinding[34]. Here, we explore its potential for TDS imaging that exploits time-domain parallax.

In our proof-of-concept demonstration, TDS is carried out by a balanced imaging system (Fig. 2a) comprising a type-II periodically poled KTiOPO$_4$ (PPKTP) crystal and two identical cameras. The linearly polarized reference pulse serves as an optical gate for sampling the detection pulse with orthogonal polarization. Optical sampling occurs twice within the same PPKTP crystal via a bidirectional sum-frequency generation process. This type-II crystal induces temporal walk-off between the detection pulse and the reference gate pulse, causing the detection pulse to be sampled twice with a small temporal offset before being captured by the respective cameras.

Two points in this scheme should be noted. First, an ultrashort pulsed laser with a well-defined, rapidly tunable repetition frequency across a broad range is essential. To achieve this, we utilize a frequency-swept electro-optical (EO) comb. In practice, to measure distance, we record the balanced signal (ΔI) while linearly sweeping the comb's f_r, and then identify the zero-crossing points during data post-processing, as illustrated in Fig. 2b. Second, the central region of the balanced curve establishes a direct correspondence between intensity and time (or intensity and displacement), enabling 3D measurements from single frames.

Experimental setup

Our setup begins with an EO comb seeded by a narrow-linewidth CW laser at 1550 nm (Fig. 3a). This comb shares a configuration similar to
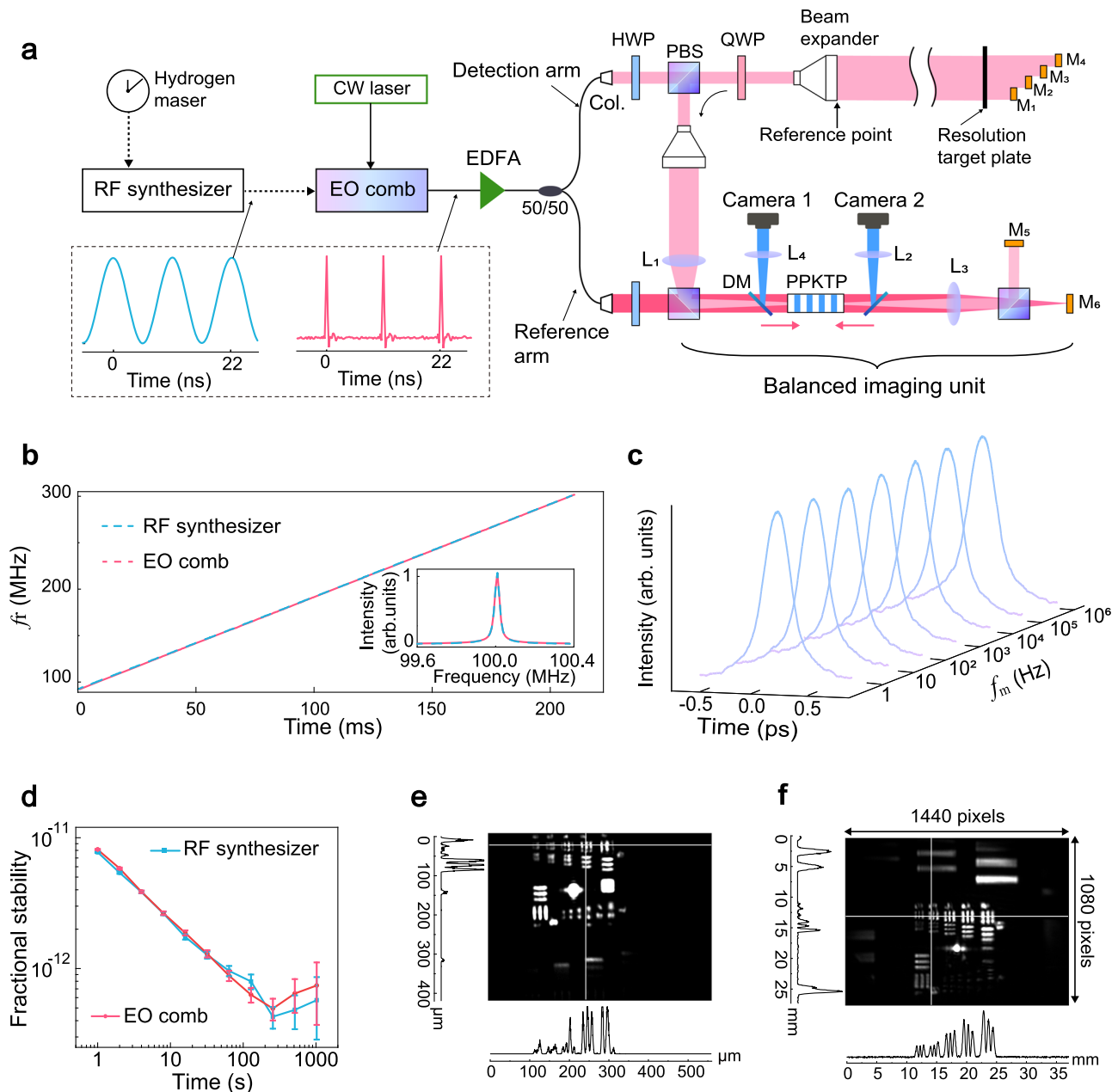
Fig. 3 | Experimental setup and characterization of the EO comb.
a Experimental setup. Col., collimator; EDFA, erbium-doped fiber amplifier; HWP, Half-wave plate; M_{1-6}, mirrors; 50/50, fiber coupler. The focus length for lenses L_1 and L_3 is 100 mm, and for L_2 and L_4 is 75 mm. The dashed box shows a 90 MHz sine wave being converted into a train of ultrashort pulses by an EO comb. **b** Linearly sweeping the comb's repetition frequency (f_r) from 90 to 300 MHz within 210 ms. Inset: RF spectra obtained by short-time Fourier transform, showing instantaneous frequencies of the RF synthesizer and the EO comb. **c** Autocorrelation traces of the EO comb versus modulation frequencies (f_m). The data is measured after the detection collimator, and the frequency deviation is fixed at 250 kHz. **d** Fractional stability of the EO comb and the RF synthesizer. The comb stability deteriorates after 200 s due to the use of fibers. **e**, **f** High-resolution and large field-of-view images of the resolution target (1951-USAF) recorded by one of the cameras. The central patterns in (**e**, **f**) correspond to groups 6 and 0, respectively.

previously reported sources[35,36], as detailed in the Methods section and Supplementary Fig. 2. Briefly, the EO comb translates a radio-frequency (RF) sinusoidal wave, generated by a hydrogen-maser-disciplined RF synthesizer, into a sequence of sub-500 fs optical pulses, using a single intensity modulator and dispersion managed nonlinear fibers. Notably, the EO comb's f_r is directly set by the RF synthesizer, offering several benefits, including the elimination of frequency locking and counting, as well as wide-range frequency tuning with high linearity (Fig. 3b). The comb's response to the RF driving signal is instantaneous, with negligible deviation within the resolution bandwidth of observation (Fig. 3b inset). Also, the comb maintains its pulse shape and temporal width when increasing the

tuning speed or the modulation frequency (f_m), as shown in Fig. 3c, showing the potential for fast measurement (discussed later). Importantly, the comb inherits the excellent frequency stability of the RF synthesizer (reaching 4×10^{-13} in 300 s, as shown in Fig. 3d), ensuring precise distance assessment.

For remote sensing, the comb output is amplified to 200 mW average power via an erbium-doped fiber amplifier (EDFA) and equally split between the detection and reference arms. In the detection light path, the comb pulses pass through a beam expander, subsequently illuminating a 3D scene with staggered mirrors and a resolution test target (1951 USAF) in front. A quarter-wave plate (QWP) and a polarization beamsplitter (PBS) serve as a free-space circulator, guiding the

reflected detection pulses to another beam expander for optical scaling, and then to the balanced imager through a second PBS, which combines the detection and orthogonally polarized reference pulses.

The balanced imaging unit comprises twin 4 f imaging systems—one with lenses L_1 and L_2, and the other with lenses L_3 and L_4—in the opposing light paths (indicated by pink arrows in Fig. 3a). The two imaging subsystems share a single type-II PPKTP crystal, where object images from both directions converge at its center in the Fourier plane. Inside, the reference pulses convert the detection pulses into sum-frequency signals at 775 nm, which are captured by two synchronized CMOS (complementary metal-oxide-semiconductor) cameras. Note that, to serve as a pump light for sum-frequency generation, the 2.2 mm diameter (full width at $1/e^2$) reference beam bounces through the crystal without focusing, minimizing spatial filtering effects on lateral resolution. As such, we achieve an optimal lateral resolution of 6 μm (limited by the crystal's transverse section) with a field-of-view (FOV) of 560×420 μm² (Fig. 3e). Currently, the 4 mm crystal (operating at room temperature) limits the acceptance angle to 3.5° (Supplementary Fig. 3) due to phase-matching restrictions commonly encountered by nonlinear optical imagers. This problem can be solved by changing the operating temperature or the poling structure of a nonlinear crystal[19,20]. Nevertheless, adjusting the magnifications of the two beam expanders in our setup allows for a broader view, such as a FOV of 3.5×2.6 cm² in Fig. 3f, at the cost of a degraded lateral resolution (315 μm) due to the cameras' fixed pixel density (1440×1080 pixels). To maintain high lateral resolution over a large FOV, high-resolution images obtained by beam steering can be stitched together, such as a full image of the 1951-USAF target (7.62×7.62 cm²) made from 46 sub-images (Supplementary Fig. 4).

Remote 3D imaging and depth measurement
First, we demonstrate TDS for 3D imaging by detecting four staggered mirror targets at a standoff distance of >1.3 m (from a reference point). Figure 4a exemplifies 2D images recorded by the two cameras at a frame rate of 165 fps (frames per second), with the comb f_r linearly changing from 165.33 to 165.60 MHz. For these images, we identify spatially correlated pixel pairs, such as points A_1 and A_2 or B_1 and B_2 (Fig. 4a), by matching corresponding features with a widely-used scale-invariant feature transform (SIFT) algorithm[37]. We then obtain the balanced signals from the paired pixels A_1A_2 and B_1B_2, as plotted in Fig. 4b. By linear fitting the central portions of the signals, we determine the zero-crossing points at 165.372 MHz and 165.510 MHz for A_1A_2 and B_1B_2, respectively. We continue tuning f_r, searching for the second zero-crossing points and calculating Δf_r as 16.54 MHz for A_1A_2 and 16.55 MHz for B_1B_2, which determine their absolute distances to be $d_0 + 1.308$ m and $d_0 + 1.3$ m, respectively. The effective optical path difference (d_0) between the detection and reference arms at the reference point in Fig. 3a is pre-calibrated to be 15.5 m.

In this measurement, we simultaneously obtain range information for dense spatial points (up to 4.67×10^7 pixel pairs), visualized as a false-color 3D point cloud in Fig. 4c. For display, the axial (z) coordinates are referenced to the point B_1B_2. Also, points lacking illumination or without a sufficient signal-to-noise ratio (SNR) are not displayed. Note that the f_r tuning step size is 606 Hz/frame, resulting in an axial resolution of 33 μm (Methods). This resolution can be improved to 54 nm with a step size of 1 Hz/frame at the cost of longer tuning time.

In another example, we perform 3D imaging on a 30%-reflective unpolished metallic foil attached to a 1-inch glass plate (Fig. 4d). This target is positioned 1.3 m away. Figure 4e presents a topographic image showing reflections from both the foil and the glass back surface. This showcases our method's ability to remotely profile metal component surfaces and complex patterns, which is applicable for industrial inspection.

Axial precision and imaging depth
Next, we assess measurement precision and accuracy by measuring the displacements of a mirror mounted on a translation stage. We compare the TDS results with the truth data obtained by a CW interferometer. Statistical analysis over 50 individual measurements (without averaging) at each displacement yields a 2-σ standard deviation (SD) within ± 10 μm, where the mean values deviate from the truth data by less than 2 μm (Fig. 5a). With 500-fold averaging, the ranging precision improves to ± 400 nm with an accuracy reaching sub-100 nm (Fig. 5b). Note that, as shown in Fig. 5c, the measured SD linearly depends on signal-to-noise ratio (SNR), which can be improved by using a high-power comb and low-noise cameras.

For further evaluation, we perform Allan deviation measurements. Experimentally, we fix the comb's f_r at a zero-crossing point, converting intensity variations of the balanced signal to deviations in distance by a conversion factor of 3.03 μm. The same factor is also used for evaluating the background noise of a camera (by blocking the comb light). Figure 5d shows the results with data acquired at a frame rate of 165 fps. Our method (data in light blue) results in a precision of ~80 nm in 25 s, which is close to the camera's noise background (in purple) and is nearly 50 times better than the unbalanced results (~4 μm, shown in pink and green) obtained by single cameras ("Methods"), demonstrating the key advantage of our method over direct ToF cameras. The off-the-shelf cameras we currently use limit the axial precision due to their moderate sensitivity and uncontrolled electronic noise. Replacing the cameras with two low-noise single-point photodetectors achieves 30 nm ranging precision in 2 s at a distance of >30 m (see Supplementary Fig. 5).

Essentially, TDS is a ranging technique, subject to dead zones dictated by the tunable range of f_r. Luckily, the EO comb, without an optical cavity, exhibits a broad tuning range of over 200 MHz, with f_r tunable from 90 to 300 MHz (Fig. 5e), limited by the bandwidth of electronics for EO comb generation. Nevertheless, this tuning range results in a dead zone of 0–0.5 m, which has been offset by the extra optical path in the detection arm and can therefore be neglected. Note that sweeping f_r across a broad range changes the comb pulse width (Fig. 5e) due to unbalanced nonlinearity and dispersion, impacting the SNR and the widths of balanced signals (Supplementary Fig. 6). However, thanks to the balanced architecture, the zero-crossing points remain unaffected, maintaining their frequencies (f_r) and separations (Δf_r). Consequently, our method permits large measurable ranges and imaging depths. An example for range imaging at a folded distance of 9.6 m is shown in Supplementary Fig. 7. With this enhanced ranging capability, our system can image objects at largely different depths. For instance, the images of two staggered objects are displayed in Fig. 5f, and their spatial separation (1.85 m) is measured. Note that, for the displayed lateral resolution of 890 μm, the theoretical DOF allowed by our imaging system is 2.4 m (Supplementary Note 1). A larger DOF can be achieved, but at the cost of reduced lateral resolution.

High-speed 3D measurement
Finally, we demonstrate the real-time measuring capability of our method, which is based on the intensity-to-displacement relationship established by fixing the f_r at a zero-crossing point. As exemplified in Fig. 6a, the highly linear region of a balanced curve (shadowed in gray) links its intensity to a target displacement (Δd), which is pre-calibrated by scanning the reference arm. Alternatively, calibration can be done without motion by sweeping the f_r ("Methods"). As such, our method enables parallel displacement and velocity measurements of moving targets within a single frame, a task that is difficult for interferometric imagers due to the complexity of signal processing.

In an experiment, we capture reflections of two mirrors (behind the 1951-USAF target) moving oppositely at similar speeds of ~5 mm/s. Using pre-calibrated intensity-to-displacement relationships (similar
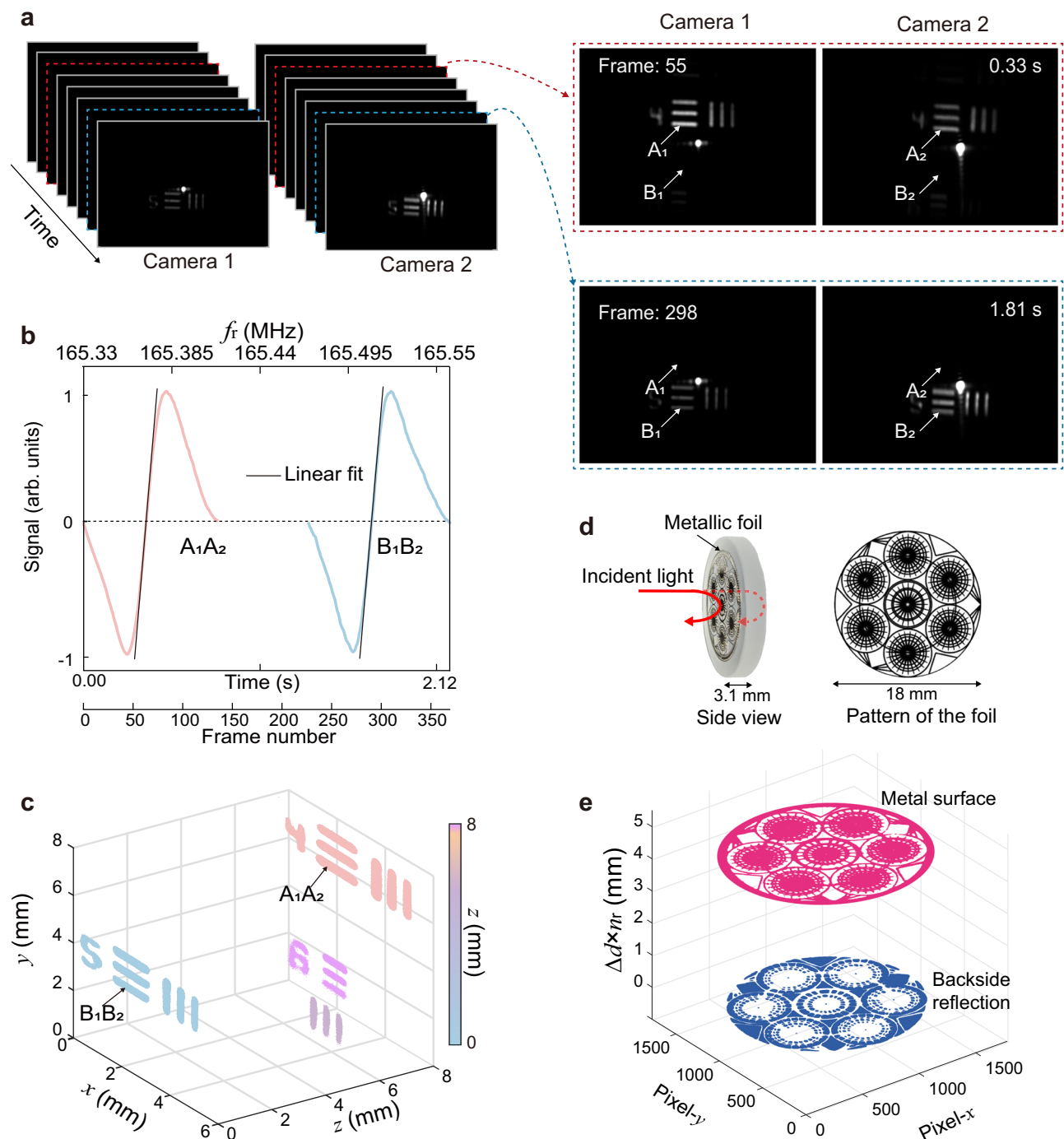
Fig. 4 | Demonstration of TDS for 3D imaging. a 2D image recorded by the cameras. **b** Balanced signals measured for pixel pairs A_1A_2 and B_1B_2. **c** 3D point cloud. Here, x, y, and z stand for spatial coordinates. The color bar represents the values in the z-axis (i.e., the depths). **d** Picture of a glass plate with a thin metallic foil attached to it. **e** Topographic imaging of the glass plate. The optical path ($\Delta d \cdot n_r$) between the foil and back surface is measured to be 4.694 mm, resulting in a plate thickness of $\Delta d = 3.128$ mm for the glass refractive index $n_r = 1.5008$.

to the one in Fig. 6a), we simultaneously measure displacements at over a million spatial points with 132 Hz data refresh rate, corresponding to a temporal resolution of 7.576 ms and a pixel rate of 205.3 megapixels/s. Figure 6b exemplifies the 3D images in motion. The trajectories of two counter-propagating imaging points (each on a mirror) are plotted in Fig. 6c, the derivatives of which reveal the instantaneous velocities of the two mirrors (Fig. 6d). Our setup currently allows a maximum measurable velocity of 330 mm/s, limited by the linear region (~ 2 mm) and the cameras' maximum frame rate (165

fps, corresponding to a pixel rate of 256.6 MHz). Employing high-speed CMOS cameras (e.g., Photron, Mini AX200, with a frame rate up to 900k fps) can increase the measurable velocity to, e.g., 520 m/s. Also, the real-time measurable displacements (< 2 mm) can be extended by rapidly tuning the f_r, which allows fast adjustment of the zero-crossing point and calibration of Δd, e.g., within 0.5 μs using high-speed photodetectors (Fig. 6e). Therefore, our method shows great potential for capturing dynamic 3D scenes, enabling studies of mechanical vibrations and deformations[38].
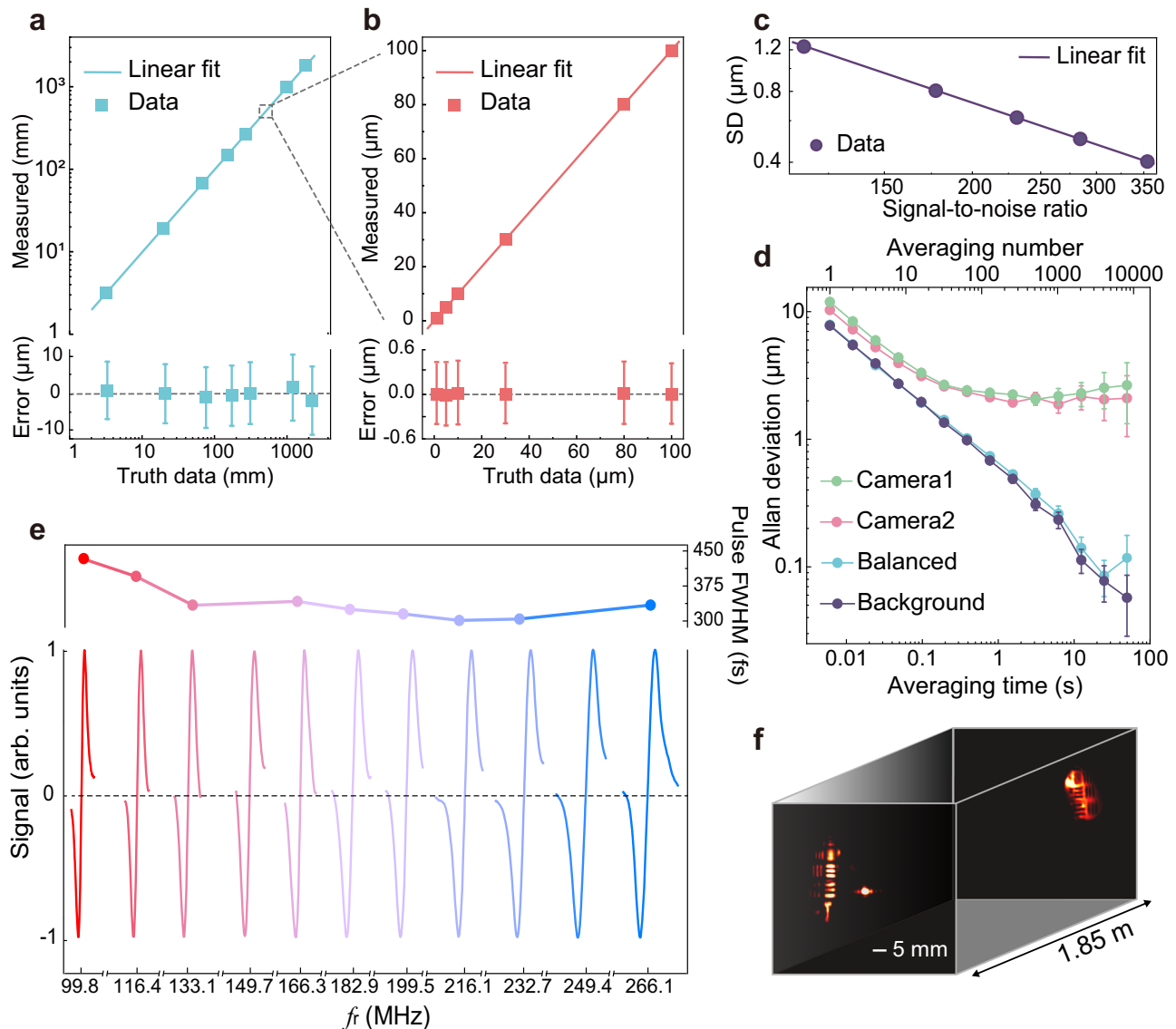
Fig. 5 | Evaluation of measurement precision and imaging depth. a Comparison measurement between our TDS imager (without averaging) and a CW laser interferometer. The offset distance is 1.3 m. **b** Measurements with 500-fold averaging. **c** Standard deviation (SD) evolving with signal-to-noise ratio (SNR). **d** Allan deviation of measurement versus averaging time (averaging number). The standoff distance is ~ 2 m. Note that the data in (**a**, **b**, and **d**) are calculated for imaging points with SNR > 300. **e** Balanced signal and EO comb pulse full width at half maximum (FWHM) recorded with tuning f_r from 90 to 300 MHz. **f** Imaging of reflections from parts of a positive (front) and a negative 1951-USAF target (behind). They separate at 1.85 m, limited by our optical platform.

Discussion

Benefiting from optical sampling and femtosecond EO comb synthesis, our system achieves sub-100 nm precision at a meter-level distance for 3D imaging. As shown in Fig. 7, the dynamic range of our setup, defined as 10·log(measurable range/precision), reaches 74 dB, underscoring its advantage over the aforementioned systems and other 3D imagers[39–44]. Besides, compared to mode-locked laser combs in some advanced lidar or imaging systems[28,30,45,46], the cavity-free EO comb in our setup offers additional merits in terms of reduced complexity, ease of operation, lower cost, and greater environmental immunity−all crucial for practical use. Also, recent advances in lithium niobate photonics have enabled on-chip fs EO comb generation[47], paving the way for a more compact and minimized system design.

Like other nonlinear optical sampling imagers[19,20], our system encounters challenges in lateral resolution, angular FOV, and, most critically, light detection efficiency. Fortunately, advancements in nonlinear optical materials and semiconductor sensors present potential solutions. For instance, larger PPKTP crystals theoretically permit higher lateral resolution, and linearly chirped ones might expand the angular FOV to, e.g., 36.7°, with minimal conversion efficiency loss (Supplementary Fig. 3). Moreover, the development of electron-multiplying CCDs has enabled nonlinear upconversion imaging at the single-photon level[20], albeit with longer integration times. This level of sensitivity enables our method to perform scanner-less range imaging, even over long distances, or in low-light conditions, as well as high-precision 3D profiling of rough, low-reflective surfaces.

With ongoing advances in semiconductor sensors and digital camera technology−particularly in pixel density, sensitivity, and speed −our method is promising for various applications[6–10], such as identifying defects on semiconductor wafers, examining crucial automotive and aerospace components for micro-level deformations, ensuring precise positioning during laser machining processes, and characterizing dynamic behaviors in micromechanical devices, among others. In addition, shifting the comb wavelength to the mid-infrared region
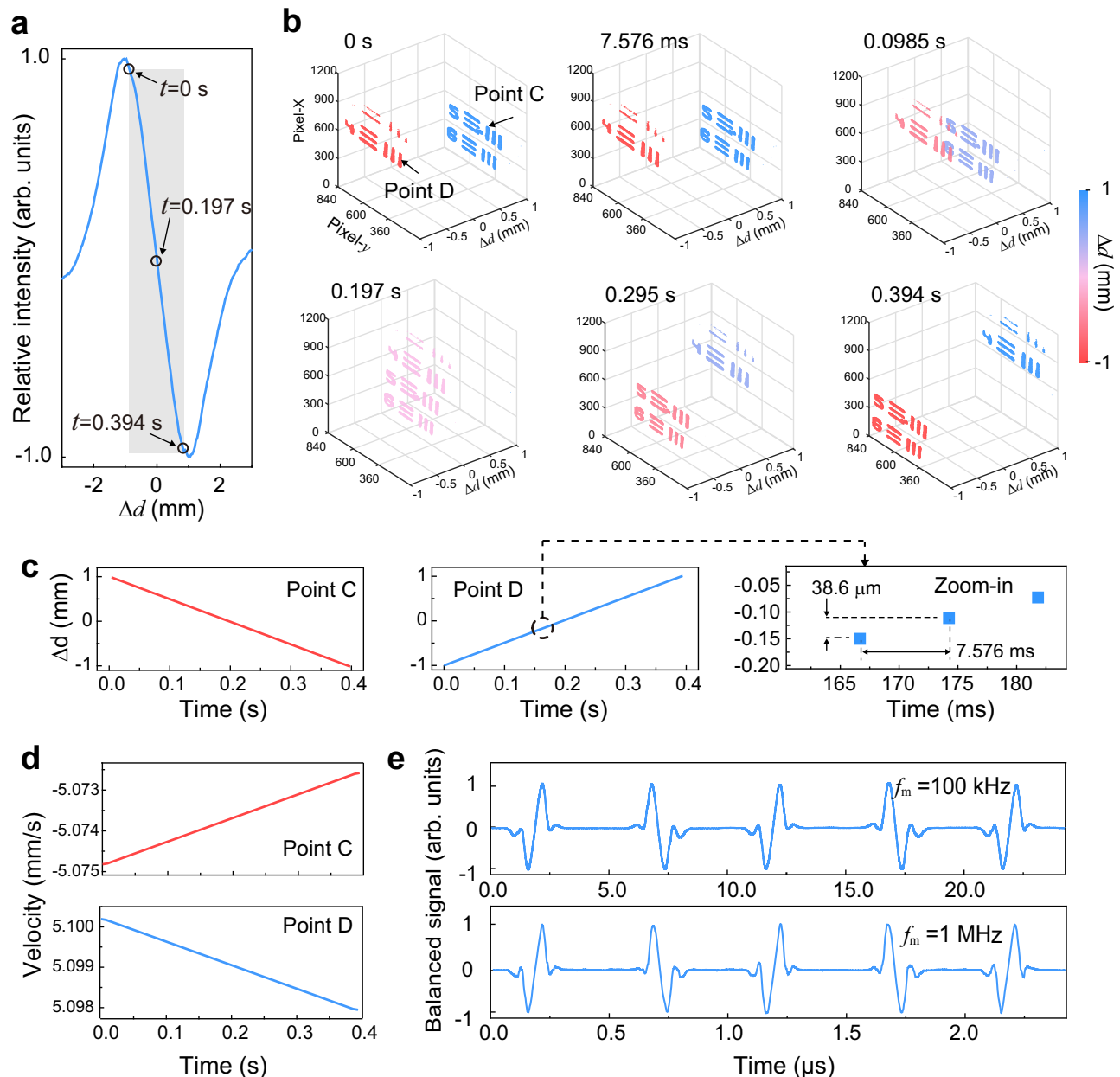
Fig. 6 | Results of rapid displacement and velocity measurements. a Balanced signal versus target displacements (Δd). **b** Rapid imaging of two targets moving towards each other. **c** Trajectories at two selected imaging points. **d** Results of velocity measurements. **e** Balanced signals recorded at modulation frequencies of $f_m = 100$ kHz and 1 MHz. For these measurements, the slow cameras are replaced by two fast photodetectors at 1 GHz bandwidth. In this case, the refresh rate of balanced signals is set by the f_m. For the frequency modulation mode, the center f_r of the EO comb is set at 165 MHz with a frequency deviation fixed at 250 kHz. Note that such a small f_r tuning range negligibly impacts the comb pulse width.

would enable broader applications in biomedical imaging and materials science[19,20].

In conclusion, we present a time-domain stereoscopic approach that offers high precision over large imaging ranges and facilitates rapid, parallel displacement and velocity measurements, thereby introducing a powerful tool for diverse 3D imaging applications.

Methods

EO comb generation
To generate the EO comb, a CW laser at 1550 nm (Adjustik E15, NKT Photonics; linewidth < 0.1 kHz; 40 mW) is fed into an intensity modulator (IM, 40 GHz bandwidth; KY-MU-15-DQ-A, Keyang Photonics), which is driven by an electrical pulse generator that converts the output of an RF synthesizer (N5173B, Keysight) into 30-ps electrical

pulses. The IM output is amplified to 150 mW using a custom-built fiber amplifier, followed by a 180 m-long dispersion-managed highly nonlinear fiber for spectral broadening. This fiber has a zero-dispersion wavelength at 1550 nm, a linear dispersion slope of 0.03 ps/(nm²·km), a loss coefficient of less than 1.5 dB/km, and a nonlinear coefficient greater than 10 W⁻¹km⁻¹. The comb pulses (-10 dB spectral width > 10 nm) are then compressed by fiber Bragg gratings, producing sub-500 fs optical pulses.

Balanced TDS imaging system
As shown in Fig. 3a, the imaging system employs two identical CMOS cameras (MV-CA016-10UM) to capture the correlated sum-frequency signals. An electrical circuit triggers the cameras in sync with the frequency tuning of the RF synthesizer. In the BCC unit, a type-II PPKTP
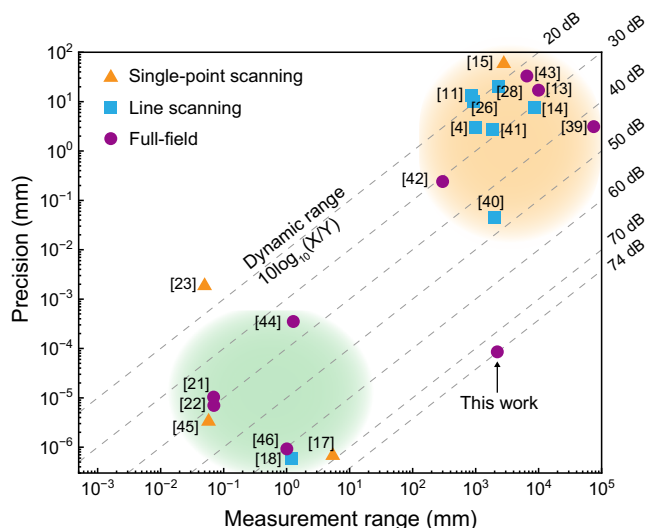
Fig. 7 | Axial precision versus measurable range for different 3D imaging systems. These systems can be classified into two groups: one characterized by high precision (marked with a green shadow) and the other by large measurement ranges (orange shadow). A trend in 3D imaging technology is the integration of these two features to broaden the scope of applications.

crystal (CASTECH, $1 \times 2 \times 4$ mm^3 for height, width, and length) is used for two key reasons. First, it creates a temporal walk-off between two orthogonally polarized pulses, necessary for balanced signal generation. To make this walk-off adjustable, an additional polarized beamsplitter (PBS) and two mirrors (M_5 and M_6 in Fig. 3a) are incorporated, with their relative positions adjustable. Note that the walk-off effect inevitably limits the sum-frequency generation efficiency (~ 0.053 mW/W^2). Further discussion is provided in Supplementary Note 1. Second, the crystal prevents second harmonic generation of each pulse, ensuring a zero background.

Calculation of SNR and axial resolution

The SNR of a balanced trace is defined as its peak value divided by the SD of a background region where the detection and reference pulses are fully separated. The axial resolution (R_z) of TDS is determined by δf, the tuning step of f_r, as $R_z = c/2n_r \cdot \Delta f_r/(f_r + \delta f) \cdot \delta f$, where the speed of light $c = 299{,}792{,}458$ m/s and the refractive index in air $n_r = 1.0003$. Therefore, we have an axial resolution of 33 μm for $\delta f = 606$ Hz/frame and 54 nm for $\delta f = 1$ Hz/frame, when $f_r = 166.3$ MHz and $\Delta f_r = 16.6$ MHz. Also, based on the above relationship, we can calibrate the curve in Fig. 6a by sweeping the f_r.

Intensity-to-displacement conversion factors

For calculating the intensity-to-displacement conversion factor, we measure a balanced trace similar to that in Fig. 6a and then linearly fit the central region, resulting in a slope of 3 μm, i.e., the conversion factor. For Allan deviation measurement with a single camera, we use a conversion factor of 6.1 μm, obtained by linear fitting the central part of the rising edge of a cross-correlation trace. We then measure the intensity fluctuations at the center point of the rising edge with a fixed f_r.

Data availability

The data used in this study are available in Zenodo under the accession code DOI link. https://doi.org/10.5281/zenodo.15863793.

References

1. Salem, R., Foster, M. A. & Gaeta, A. L. Application of space–time duality to ultrahigh-speed optical signal processing. *Adv. Opt. Photonics* **5**, 274–317 (2013).
2. Fard, A. M., Gupta, S. & Jalali, B. Photonic time-stretch digitizer and its extension to real-time spectroscopy and imaging. *Laser Photonics Rev.* **7**, 207–263 (2013).
3. Mahjoubfar, A. et al. Time stretch and its applications. *Nat. Photon.* **11**, 341–351 (2017).
4. Jiang, Y., Karpf, S. & Jalali, B. Time-stretch LiDAR as a spectrally scanned time-of-flight ranging camera. *Nat. Photon.* **14**, 14–18 (2020).
5. Lambooij, M., Ijsselsteijn, W., Bouwhuis, D. G. & Heynderickx, I. Evaluation of stereoscopic images: beyond 2d quality. *IEEE Trans. Broadcast.* **57**, 432–444 (2011).
6. Li, N. et al. A progress review on solid-state LiDAR and nanophotonics-based LiDAR sensors. *Laser Photonics Rev.* **16**, 2100511 (2022).
7. Kim, I. et al. Nanophotonics for light detection and ranging technology. *Nat. Nanotechnol.* **16**, 508–524 (2021).
8. Horaud, R., Hansard, M., Evangelidis, G. & Ménier, C. An overview of depth cameras and range scanners based on time-of-flight technologies. *Mach. Vis. Appl.* **27**, 1005–1020 (2016).
9. Xia, R. et al. Detection method of manufacturing defects on aircraft surface based on fringe projection. *Optik* **208**, 164332 (2020).
10. Kaul, L., Zlot, R. & Bosse, M. Continuous-time three-dimensional mapping for micro aerial vehicles with a passively actuated rotating laser scanner. *J. Field Robot.* **33**, 103–132 (2016).
11. Stellinga, D. et al. Time-of-flight 3D imaging through multimode optical fibers. *Science* **374**, 1395–1399 (2021).
12. Zhang, S. High-speed 3d shape measurement with structured light methods: A review. *Opt. Lasers Eng.* **106**, 119–131 (2018).
13. Zhang, X. et al. A large-scale microelectromechanical-systems-based silicon photonics LiDAR. *Nature* **603**, 253–258 (2022).
14. Li, B., Lin, Q. & Li, M. Frequency–angular resolving LiDAR using chip-scale acousto-optic beam steering. *Nature* **620**, 316–322 (2023).
15. Snigirev, V. et al. Ultrafast tunable lasers using lithium niobate integrated photonics. *Nature* **615**, 411–417 (2023).
16. Nwaneshiudu, A. et al. Introduction to confocal microscopy. *J. Investig. Dermatol.* **132**, 1–5 (2012).
17. Na, Y. et al. Ultrafast, sub-nanometre-precision and multifunctional time-of-flight detection. *Nat. Photon.* **14**, 355–360 (2020).
18. Na, Y. et al. Massively parallel electro-optic sampling of space-encoded optical pulses for ultrafast multi-dimensional imaging. *Light Sci. Appl.* **12**, 44 (2023).
19. Fang, J. et al. Mid-infrared single-photon 3D imaging. *Light Sci. Appl.* **12**, 144 (2023).
20. Huang, K. et al. Wide-field mid-infrared single-photon upconversion imaging. *Nat. Commun.* **13**, 1077 (2022).
21. Joo, W.-D. et al. Femtosecond laser pulses for fast 3-D surface profilometry of microelectronic step-structures. *Opt. Express* **21**, 15323–15334 (2013).
22. Wang, Y. et al. Large-field step-structure surface measurement using a femtosecond laser. *Opt. Express* **28**, 22946–22961 (2020).
23. Zvagelsky, R. et al. Towards in situ diagnostics of multi-photon 3D laser printing using optical coherence tomography. *Light Adv. Manuf.* **3**, 39 (2022).
24. Kumar, U. P. et al. White light interferometry for surface profiling with a colour CCD. *Opt. Lasers Eng.* **50**, 1084–1088 (2012).
25. Coddington, I. et al. Rapid and precise absolute distance measurements at long range. *Nat. Photon.* **3**, 351–356 (2009).
26. Lukashchuk, A. et al. Chaotic microcomb-based parallel ranging. *Nat. Photon.* **17**, 814–821 (2023).
27. Li, R. et al. Ultra-rapid dual-comb ranging with an extended non-ambiguity range. *Opt. Let.* **47**, 5309–5312 (2022).
28. Riemensberger, J. et al. Massively parallel coherent laser ranging using a soliton microcomb. *Nature* **581**, 164–170 (2020).
29. Vicentini, E. et al. Dual-comb hyperspectral digital holography. *Nat. Photon.* **15**, 890–894 (2021).

30. Hase, E. et al. Scan-less confocal phase imaging based on dual-comb microscopy. *Optica* **5**, 634–643 (2018).
31. Kim, J., Chen, J., Cox, J. & Kärtner, F. X. Attosecond-resolution timing jitter characterization of free-running mode-locked lasers. *Opt. Lett.* **32**, 3519–3521 (2007).
32. Benedick, A., Fujimoto, J. & Kärtner, F. Optical flywheels with attosecond jitter. *Nat. Photon.* **6**, 97–100 (2012).
33. Xin, M. et al. Attosecond precision multi-kilometer laser-microwave network. *Light Sci. Appl.* **6**, e16187 (2017).
34. Lee, J. et al. Time-of-flight measurement with femtosecond light pulses. *Nat. Photon.* **4**, 716–720 (2010).
35. Millot, G. et al. Frequency-agile dual-comb spectroscopy. *Nat. Photon.* **10**, 27–30 (2016).
36. Lv, T. et al. Ultrahigh-speed coherent anti-stokes Raman spectroscopy with a hybrid dual-comb source. *ACS Photonics* **10**, 2964 (2023).
37. Lowe, D. G. Object recognition from local scale-invariant features. In *Proceeding of the Seventh IEEE International Conference on Computer Vision* **2**, 1150–1157 (1999).
38. Kakue, T. et al. Digital holographic high-speed 3D imaging for the vibrometry of fast-occurring phenomena. *Sci. Rep.* **7**, 10413 (2017).
39. Rogers, C. et al. A universal 3D imaging sensor on a silicon photonics platform. *Nature* **590**, 256–261 (2021).
40. Qian, R. et al. Video-rate high-precision time-frequency multiplexed 3D coherent ranging. *Nat. Commun.* **13**, 1476 (2022).
41. Chen, R. et al. Breaking the temporal and frequency congestion of LiDAR by parallel chaos. *Nat. Photon.* **17**, 306–314 (2023).
42. Jing, X. et al. Single-shot 3D imaging with point cloud projection based on metadevice. *Nat. Commun.* **13**, 7842 (2022).
43. Choi, E. et al. 360° structured light with learned metasurfaces. *Nat. Photon.* **18**, 848–855 (2024).
44. Kato, T., Uchida, M., Tanaka, Y. & Minoshima, K. High-resolution 3D imaging method using chirped optical frequency combs based on convolution analysis of the spectral interference fringe. *OSA Contin.* **3**, 20 (2020).
45. Xu, G. Y. et al. Digital-micromirror-device-based surface measurement using heterodyne interferometry with optical frequency comb. *Appl. Phys. Lett.* **118**, 251104 (2021).
46. Zhang, W. et al. Comb-referenced frequency-sweeping interferometry for precisely measuring large stepped structures. *Appl. Opt.* **57**, 1247–1253 (2018).
47. Yu, M. et al. Integrated femtosecond pulse generator on thin-film lithium niobate. *Nature* **612**, 252–258 (2022).

Acknowledgements

Author contributions

M.Y. and H.Z. conceived the idea and designed the experiments. Z.W. and H.M. conducted the experiment and drafted the manuscript. Z.W., H.M., and J.L. analyzed the data. M.Y., K.H. and J.F. build the comb source. M.Y., H.Z., J.G. and K.H. revised the manuscript. All authors provided comments and suggestions for improvements.

Competing interests

The authors declare no competing interests.

Additional information

Supplementary information The online version contains supplementary material available at https://doi.org/10.1038/s41467-025-62228-5.

Correspondence and requests for materials should be addressed to Ming Yan or Heping Zeng.

Peer review information *Nature Communications* thanks the anonymous reviewer(s) for their contribution to the peer review of this work. A peer review file is available.

Reprints and permissions information is available at http://www.nature.com/reprints

Publisher's note Springer Nature remains neutral with regard to jurisdictional claims in published maps and institutional affiliations.